Importance of quadratic dispersion in acoustic flexural phonons for thermal transport of two-dimensional materials

Armin Taheri
Department of Electrical Engineering and Computer Science, York University, Toronto, Ontario, Canada M3J1P3

Simone Pisana
Department of Electrical Engineering and Computer Science, York University, Toronto, Ontario, Canada M3J1P3 and Department of Physics and Astronomy, York University, Toronto, Ontario, Canada M3J1P3

Chandra Veer Singh*
Department of Materials Science and Engineering, University of Toronto, Toronto, Ontario, Canada M5S3E4

(Received 22 April 2021; revised 7 June 2021; accepted 10 June 2021; published 22 June 2021)

Solutions of the Peierls-Boltzmann transport equation using inputs from density functional theory calculations have been successful in predicting the thermal conductivity in a wide range of materials. In the case of two-dimensional (2D) materials, the accuracy of this method can depend highly on the shape of the dispersion curve for flexural phonon (ZA). As a universal feature, very recent theoretical studies have shown that the ZA branch of 2D materials is quadratic. However, many prior thermal conductivity studies and conclusions are based on a ZA branch with linear components. In this paper, we systematically study the impact of the long-wavelength dispersion of the ZA branch in graphene, silicene, and α-nitrophosphorene to highlight its role on thermal conductivity predictions. Our results show that the predicted κ value, its convergence and anisotropy, as well as phonon lifetimes and mean free path can change substantially even with small linear to pure quadratic corrections to the shape of the long-wavelength ZA branch. Also, having a pure quadratic ZA dispersion can improve the convergence speed and reduce uncertainty in this computational framework when different exchange-correlation functionals are used in the density functional theory calculations. Our findings may provide a helpful guideline for more accurate and efficient thermal conductivity estimation in mono- and few-layer 2D materials.

DOI: 10.1103/PhysRevB.103.235426

I. INTRODUCTION

Triggered by the successful isolation of graphene and its unique characteristics, the study of single-layer and few-layer two-dimensional (2D) materials has become the main focus of many research activities in materials science and condensed matter physics over the past two decades. Their features such as a large surface-to-volume ratio, structural stability, ability to readily be combined into heterostructures, and a promising combination of electronic, optical, and thermal properties have made them ideally suited to modern devices. However, fulfilling many of these potentials for targeted applications such as optoelectronics, thermoelectrics, thermal spreading, and interface materials closely depends on having a fundamental understanding of the physics of thermal transport in these atomically thin systems. Particularly, it is crucial to have an accurate estimation of their lattice thermal conductivity κ, as it determines how effectively can spatially localized heat be eliminated from the device. Furthermore, the use of materials in highly integrated devices requires an understanding of nondiffusive heat transport phenomena, which become prevalent at the nanoscale. Thus, many prior studies have focused on the investigation of different aspects of thermal transport in 2D materials by means of theoretical and experimental techniques. Based on these studies, 2D materials offer a broad spectrum of room-temperature thermal conductivity, from very low values such as 0.26 $\mathrm{W\,m^{-1}\,K^{-1}}$ in PbSe monolayer [1] to the high thermal conductivity shown in graphene of 5300 $\mathrm{W\,m^{-1}\,K^{-1}}$ [2], attractive for both thermoelectric and thermal management applications.

Within the theoretical approaches commonly used to predict the thermal conductivity of 2D materials or to further interpret available experimental measurements, solving the Peierls-Boltzmann transport equation (PBTE) with interatomic force constants (IFCs) obtained from density functional theory (DFT) calculations has become a powerful tool [1,3–9]. Apart from its high accuracy, one of the striking advantages of the PBTE/DFT method over other theoretical approaches such as simulations of molecular dynamics (MD) is its predictive power, as it does not depend on empirical interatomic potentials. which have not yet been parameterized for many novel systems. However, there are also challenges with the application of first-principles PBTE/DFT calculation in nanostructured materials [10]. One of the main issues of this method is the fact that the accuracy of the predicted κ value depends highly on the accuracy of the second- and third-order IFCs obtained from DFT, which in turn depend

*chandraveer.singh@utoronto.ca

on careful optimization of parameters such as the choice of the exchange-correlation functional (XCF) and type of the pseudopotential (PP), cutoff energy for wave functions, size of the supercell, cutoff radius, and **k**-point grid. Convergence tests do not always provide a means to correct errors originating from choosing overly conservative parameters that can mitigate the computational cost. Even small errors in IFCs can propagate into large inaccuracy in predicted phonon lifetime, group velocity, and thermal conductivity. Although a few previous studies [11–14] provide helpful insight into the effect of one or two of these factors in the accuracy of the predicted κ value, simultaneous consideration of the effect of all these contributing factors in the accuracy of PBTE/DFT κ calculation seems an extremely computationally expensive task.

In the case of 2D materials, the accuracy of the harmonic IFCs and dispersion curve, particularly the acoustic out-of-plane flexural (ZA) phonon dispersion, can pose additional challenges in PBTE/DFT κ calculation, which are not encountered in bulk systems. It is well known that the long-wavelength ZA phonons play a central role in determining many properties of 2D materials such as phonon thermal transport [2], electron-phonon coupling [15], thermodynamic stability [16], and bending mechanics [17]. Predicted by continuum elasticity theory [18] as a universal feature, the ZA branch in monolayers and van der Waals (VdW) multilayer systems has purely quadratic dispersion. However, the general nature of the ZA dispersion of low-dimensional materials in the long-wavelength limit has remained to be a long-lasting debate both experimentally [19] and theoretically [20,21]. Many DFT calculations report a linear ZA branch close to the Γ point for 2D materials such as silicene [22,23], phosphorene [6], MoS_2 [24], WS_2 [25], D-graphene [26], T-graphene [26], and WSe_2 [27], while other studies on the same 2D materials report a quadratic ZA branch (silicene [28], phosphorene [29], WS_2 [30]). As one of the first microscopic attempts to clarify the situation in atomistic systems, a study by Carrete *et al.* [21] suggested that the ZA branch in unstrained 2D materials, whether they are planar or buckled, is purely quadratic. In that study, they developed a reformulation of the second-order IFCs in terms of internal coordinates, which adds a post-processing step to the "raw" harmonic IFCs obtained from common DFT packages to enforce the necessary and sufficient conditions for rotational symmetry, which first were formulated by Born and Huang [31] and later modified by Gazis and Wallis [32], and Wang *et al.* [33]. These conditions ensure that the potential energy of the system and the force acting on each particle in the absence of external fields remains invariant under rigid rotation. In Ref. [21], the presence of linear components in the ZA branch of some 2D materials predicted by previous studies was also attributed to the possible violation of the rotational symmetry conditions. furthermore, in another recent analytical study based on lattice chain theory, Kuang *et al.* [20] showed that the ZA branch in covalent and van der Waals monolayer and multilayer 2D lattices has quadratic dispersion, independent of their backbone geometry.

The behavior of the ZA mode in the long-wavelength limit (whether quadratic or linear) can substantially affect different aspects of phonon thermal transport in 2D materials, including the predicted κ value, its convergence or divergence in the limit of infinite system size, and even its anisotropy. As a common problem, the ZA dispersion near the center of the Brillouin zone obtained from the raw IFCs calculated using common software packages shows either linear components or, in severe cases, a small U-shaped region with imaginary frequencies. This can be attributed to either structure-related reasons such as hybridization between the polarization of the TA/LA modes with the ZA mode, which usually occurs in nonplanar 2D materials, or to DFT-related reasons such as using periodic boundary conditions along different axes, and numerical inaccuracies caused by insufficient cutoff values and not large enough supercell adopted in the calculations. All of these can lead to a breakdown of the rotation symmetry and lead to nonquadratic ZA branch. Unfortunately, except for a few cases, many previous works that studied different aspects of thermal transport in 2D materials by the PBTE/DFT method have been performed using the raw IFCs directly obtained from DFT packages, with the possibility of violation of the rotational invariance constraint. For example, based on two studies using the PBTE/DFT method, one by Xie *et al.* [34], and another one by Gu and Yang [23], the intrinsic thermal conductivity of unstrained silicene diverges with denser **q**-mesh. However, inspection of their phonon dispersion shows that their ZA branch close to the Γ point has linear components. In another study by Kuang *et al.* [35] with the same methodology, the intrinsic κ of infinite unstrained silicene converged with increasing **q**-point grid points. The dispersion curve used in [35] is more quadratic than [23] and [34], but still is not purely quadratic. Thus, naturally, questions arise such as what the true value and convergence/divergence behavior of κ in silicene is, and whether enforcing a perfectly quadratic ZA curve during PBTE/DFT calculations is a rigorous computational approach. Another important research question when using the PBTE/DFT calculation framework to predict κ has been about the effect of different exchange-correlation functional and pseudopotential types on the final predicted value of κ. Regarding 2D materials, Taheri *et al.* [11] and Qin *et al.* [12] used different exchange-correlation functionals to study κ of graphene as a benchmark. Based on their results, using different exchange-correlation functional leads to a considerable diversity on the predicted κ value, in the range of 1936–4376 $W\,m^{-1}K^{-1}$ according to [12], and 5442–8677 $W\,m^{-1}\,K^{-1}$ according to [11]. In both studies, the wide range of predicted κ values is attributed to the considerable difference in the phonon lifetimes at the long-wavelength limit predicted by different exchange-correlation functionals. However, investigation of the phonon dispersion curves presented by these studies also reveals the possible presence of linear components in the ZA dispersion at the long-wavelength limit, resulting in nonzero group velocity at Γ. So, this may raise an open question whether enforcing the rotational invariance before thermal conductivity calculation on the raw harmonic IFCs obtained by each exchange-correlation functional to get a purely quadratic ZA dispersion leads to more consistent predicted κ value in 2D materials.

In this paper, we revisit the phonon thermal transport in 2D monolayers including graphene, silicene, and α-nitrophosphorene (α-NP) as representative 2D structures with flat, buckled, and puckered backbone geometries,

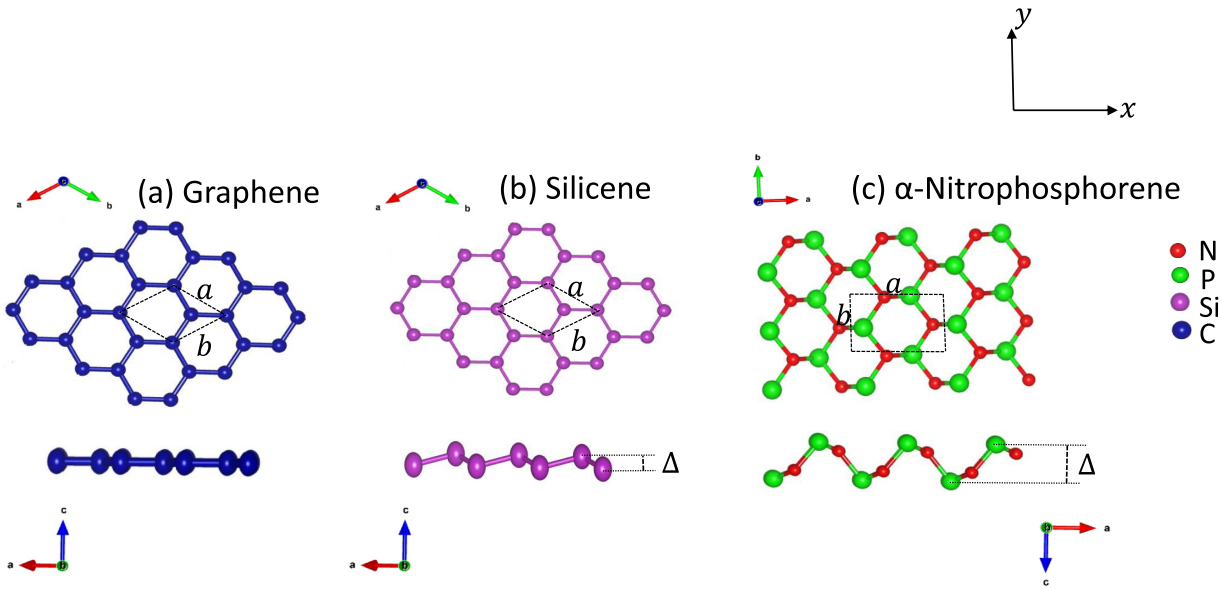

FIG. 1. The unit cell, and top and side views of supercells of (a) graphene, (b) silicene, and (c) α-NP. The lattice constants are shown as a and b, and the puckering/buckling distance is denoted by Δ. The x and y directions are also shown.

respectively. The results of black phosphorene is also presented in the the Supplemental Material [36]. In each case, PBTE/DFT κ calculations are performed based on both commonly used raw harmonic IFCs directly obtained from DFT packages as well as postprocessed corrected IFCs, which fully satisfy the rotational invariance constraint. The dominant effects of this correction on various fundamental aspects of thermal transport in 2D materials such as κ value and its anisotropy, convergence/divergence, and uncertainty with respect to using different XCFs are systematically studied.

II. COMPUTATIONAL METHODS

As the first step in the PBTE/DFT κ calculation workflow, the unit cell of the three monolayers studies here are fully relaxed using the Quantum Espresso (QE) package to obtain the optimized lattice vectors and atomic positions. Except for graphene, where different exchange-correlation functionals are tested, we use a Perdew–Burke–Ernzerhof (PBE) exchange-correlation functional with a projected augmented wave (PAW) pseudopotential for DFT calculations. The electronic wave functions are expanded with plane waves up to an energy cutoff of 110 Ry. An electronic **k**-point mesh of $31 \times 31 \times 1$ centered at Γ is used for reciprocal space integration of the Brillouin zone (BZ). The energy and force convergence thresholds in geometry relaxation are set to 10^{-11} a.u. and 10^{-10} a.u., respectively. We also use a vacuum spacing of 20 Å along the z axis to eliminate artificial interactions between neighboring layers. Figure 1 shows the optimized unit cell and a supercell of the different monolayers considered in this work. Summarized in Table I are also the optimized lattice constants (a and b) and the puckering/buckling distance (Δ) for each structure. Our results are found to be in good agreement with previously reported values [37–39].

Having obtained the relaxed geometrical parameters for each monolayer, the harmonic phonon calculations are then performed to obtain the second-order IFCs and phonon dispersion curves using the PHONOPY package [40]. We compute the second-order harmonic IFCs in $8 \times 8 \times 1$, $8 \times 8 \times 1$, and $10 \times 10 \times 1$ supercells for graphene, silicene, and α-NP, respectively. We use the term "raw" throughout this paper to refer to the harmonic IFCs directly obtained from PHONOPY at this step, with no further correction. After obtaining the raw harmonic IFCs, we use the method proposed in Ref. [41] using the HiPhive package to enforce the rotational invariance conditions. Here we briefly explain the general idea behind the postprocessing approach to enforce, for example, the rotational invariance. Having obtained the harmonic IFCs $\widetilde{\mathbf{a}}$ and rotational constraint matrix $\mathbf{C}^{\text{rot}}$, if the rotational invariance is satisfied then $\mathbf{C}^{\text{rot}}\widetilde{\mathbf{a}} = 0$. However, usually, the $\widetilde{\mathbf{a}}$ obtained from DFT packages does not satisfy this condition, and $\mathbf{C}^{\text{rot}}\widetilde{\mathbf{a}} = \mathbf{d}$, where $\mathbf{d}$ is a parameter that shows how well the IFCs satisfy the rotational constraint. To address this, a set of corrections $\Delta\widetilde{\mathbf{a}}$ are defined such that $\mathbf{C}^{\text{rot}}(\widetilde{\mathbf{a}} + \Delta\widetilde{\mathbf{a}}) = 0$. The problem then becomes finding the set of $\Delta\widetilde{\mathbf{a}}$, subject to the constraint $||\mathbf{C}^{\text{rot}}\Delta\widetilde{\mathbf{a}} + \mathbf{d}|| < \epsilon_1$ and $||\Delta\widetilde{\mathbf{a}}|| < \epsilon_2$, where ϵ_1 and ϵ_2 are numerical tolerance parameters. This problem can then be solved for example by ridge regression using the $l_2 -$ norm. More details about this method can be found in Ref. [41].

Next, we calculate the third-order anharmonic IFCs using the finite difference method implemented in the thirdorder.py script [42]. We use $9 \times 9 \times 1$, $9 \times 9 \times 1$, and $5 \times 5 \times 1$ supercells for graphene, silicene, and α-NP, respectively. Also, the atomic interactions are considered up to the eighth-nearest neighbor in graphene and silicene, and up to the tenth-nearest neighbor in α-NP.

Finally, having obtained the second-order and third-order IFCs the lattice thermal conductivity based on the iterative solution is expressed as

$$\kappa_l^{\alpha\alpha} = \frac{1}{k_B T^2 \Omega N^2} \sum_{\lambda(\mathbf{q},p)} n_\lambda^0 \left(1 + n_\lambda^0\right) (\hbar\omega_\lambda)^2 v_\lambda^\alpha F_\lambda^\alpha, \qquad (1)$$

TABLE I. The calculated lattice constants (a and b) and puckering/buckling height (Δ) in 2D crystals considered in this study. All results are obtained using a PBE exchange-correlation functional with a PAW pseudopotential.

Material	a(Å)	b(Å)	Δ(Å)
Graphene	2.47	2.47	
Silicene	3.87	3.87	0.45
α-NP	4.17	2.71	1.90

where k_B is Boltzmann's constant, T is the temperature, Ω denotes the unit-cell volume, N^2 is the total number of $\mathbf{q}$-point mesh used for the first BZ integration ($N \times N \times 1$ $\mathbf{q}$-point grid), $\lambda(\mathbf{q}, p)$ represents a phonon mode with wave vector $\mathbf{q}$ and polarization branch number p, n^0_λ is the phonon occupation number based on Bose-Einstein statistics, ω is the phonon frequency, $\hbar$ is the reduced Plank constant, v^α_λ represents the phonon group velocity in the direction α, and F_λ is given by

$$\mathbf{F}_\lambda = \tau^0_\lambda(\mathbf{v}_\lambda + \mathbf{\Delta}_\lambda), \tag{2}$$

in which τ^0_λ is the relaxation time of mode λ and $\mathbf{\Delta}_\lambda$ is a correction term with the dimension of velocity. Other details about this method can be found in Ref. [42]. Also, we use the thicknesses of 3.35 Å [3], 4.20 Å [35], and 6.35 Å [43,44] for graphene, silicene, and α-NP, respectively.

III. RESULT AND DISCUSSION

A. Graphene

We first consider graphene as the most well-known 2D material with a flat, planar lattice structure. Despite the extensive experimental and theoretical research efforts during the last decade, many aspects of phonon thermal transport in monolayer and multilayer graphene such as the uncertainty in the value of lattice thermal conductivity, its convergence behavior, the effect of higher-order phonon-phonon processes, and finite temperature effects are still active topics of study. Here we focus on the effects that correcting IFCs obtained from DFT packages using the postprocessing approach discussed in Sec. II can have on phonon thermal transport in freestanding infinite monolayer graphene. Figure 2(a) shows the phonon dispersion curve of graphene using both raw and corrected IFCs. As there are two atoms in its unit cell, the dispersion curve of graphene consists of six total modes, three of which are acoustic modes (labeled as ZA, TA, and LA) and the rest are optical modes. With the scales of Fig. 2(a), for all phonon modes the two dispersion curves are visually indistinguishable; both show no negative frequencies in the vicinity of the Γ point, the ZA mode at the long-wavelength limit for both IFCs seems quadratic, and the TA and LA modes in the same limit are linear. However, a careful investigation of phonon frequencies in the regions very close to the Γ point in both Γ-M and Γ-K directions reveals that the ZA branch obtained by raw IFCs deviates from a pure quadratic dispersion, and contain linear components. This can be better seen in Figs. 2(b) and 2(c), which show detail of the phonon dispersion curves in the vicinity of the Γ point along the Γ-M and Γ-K directions, respectively. For example, as shown in Fig. 2(b), a fit of $\omega(\mathbf{q})$ for the ZA phonon mode obtained from the raw IFCs for $0 < \mathbf{q} < 0.06$ in the Γ-M high-symmetry direction gives a linear coefficient $\omega = 6.46q$, while the ZA branch obtained from the corrected IFCs perfectly fits a quadratic relation as $\omega = 76.79q^2 + 0.0004q$, which has a negligible linear component. We also note that except this difference in the ZA mode, other phonon modes including TA, LA, and optical phonons remain perfectly unchanged after the correction.

Next, we consider the phonon group velocity obtained using the raw and corrected IFCs. Here we focus on acoustic modes as they have much larger group velocity compared to

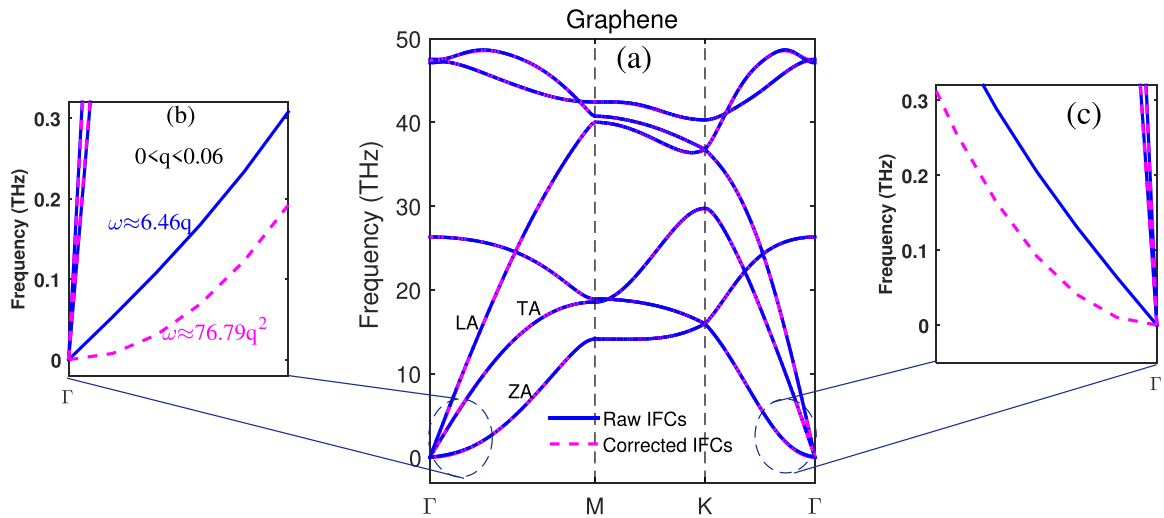

FIG. 2. (a) Phonon dispersion curve of graphene using raw and corrected harmonic IFCs. (b) Zoomed-in dispersion close to Γ along the Γ-M direction. (c) Zoomed-in dispersion close to Γ along the Γ-K direction.

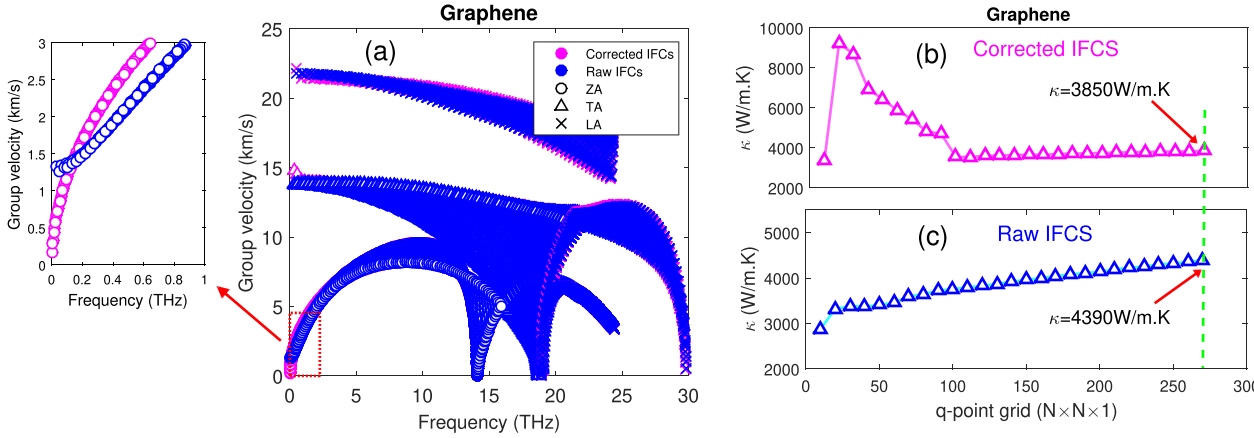

FIG. 3. (a) Group velocity of acoustic modes in graphene. [(b) and (c)] Convergence of thermal conductivity of graphene at 300 K with respect to **q**-point grid size predicted by the corrected and raw harmonic IFCs, respectively.

the optical modes, and are known to dominate the phonon thermal transport in graphene. As group velocity is defined as $v_g = \frac{d\omega}{d\mathbf{q}}$, we expect that the correction of IFCs also affects the group velocity of the ZA mode close to the Γ point. Figure 3(a) shows the group velocity of acoustic modes over the entire Brillouin zone in graphene. The quadratic nature of the ZA mode close to the Γ point imposes a zero group velocity for this mode at Γ. However, based on Fig. 3(a), the linear components of the ZA dispersion at the long-wavelength limit obtained from the raw IFCs leads to a nonzero group velocity of about 1.3 km/s for this mode. This nonzero group velocity vanishes at Γ when corrected IFCs are used, as a result of the strictly quadratic shape of the ZA branch close to this point [Figure 2(b)]. Except for the case of the ZA mode at the long-wavelength limit, the maximum change in the group velocity of other phonons obtained from raw or corrected IFCs is less than 5%.

Now we consider the convergence behavior of the thermal conductivity when the raw or corrected second-order harmonic IFCs are used. The question of whether thermal conductivity of infinite size free standing graphene considering only three-phonon scattering process converges or not has been a very controversial topic experimentally [2,45] and theoretically by means of MD [46,47] and DFT [3,48] thermal conductivity calculations frameworks. Figures 3(b) and 3(c) show the convergence behavior of room-temperature lattice thermal conductivity in free-standing infinite graphene using the iterative solution in the PBTE/DFT method based on the corrected and raw harmonic IFCs. The anharmonic third-order IFCs used in the calculations for both cases are the same. Very interestingly, we found that the seemingly small change in the behavior of the ZA modes close to Γ after enforcement of the invariance rules drastically affects the convergence behavior of the predicted κ. Based on Fig. 3(b), the κ value obtained using the corrected IFCs is well converged with respect to increase in size of the **q**-point mesh used to integrate over the BZ. As can be seen in Fig. 3(b), a $100 \times 100 \times 1$ **q**-point mesh is sufficient to converge the value of κ, and further increase in **q**-point mesh results in less than 5% change in thermal conductivity. Recently, Kuang *et al.* [48] also reported the convergence of thermal conductivity of infinite graphene only considering three-phonon processes, but based on their results the convergence is achieved using an extremely dense **q**-point mesh of $301 \times 301 \times 1$ in the calculations. As the size of the **q**-point mesh used in thermal conductivity calculation step within PBTE/DFT method greatly affects the computational cost and memory requirement, our results suggest that by correcting the harmonic IFCs one can also gain considerable computational efficiency. Now, we consider the convergence behavior of the lattice thermal conductivity obtained by using raw IFCs, as shown in Fig. 3(c). Contrary to the case of corrected IFCs, it can be seen that κ increases almost linearly with the size of **q**-point grid. So, based on our findings, we attribute the logarithmic divergence of intrinsic κ in graphene reported in the prior studies to possible violation of rotational symmetry of the ZA mode. For the sake of comparison, we also calculate the value of lattice thermal conductivity in a very dense grid of $270 \times 270 \times 1$ in these two cases. The κ value obtained using the raw and corrected IFCs at 300 K are 4390 $\mathrm{W\,m^{-1}\,K^{-1}}$ and 3850 $\mathrm{W\,m^{-1}\,K^{-1}}$, respectively. We will compare these values to experimental data in the literature later. To better shed light onto the reason for this difference in the convergence of thermal conductivity, we consider the phonon lifetime of acoustic modes as shown in Fig. 4(a). Based on our results, the correction of the harmonic IFCs mostly affects the lifetimes of the ZA phonons at the long-wavelength limit, as they become shortened by about two orders of magnitudes compared to the lifetime obtained by raw IFCs, similar to the case of borophene [21]. At frequencies higher than 1 THz, the phonon lifetimes of all acoustic modes practically remain unchanged after the correction. Usually, the phonon lifetime of the ZA mode at the long-wavelength limit scales by a power-law relation with frequency as $\tau = \beta\omega^{-\gamma}$, where β and γ are strain-dependent parameters. It was shown that the divergence of the thermal conductivity occurs when $\gamma > 2$ [47,48]. Our numerical fitting shows that the value of γ is 2.70 and 0.16 for raw and corrected IFCs, respectively. This explains the divergence and convergence behavior observed in thermal conductivity using raw and corrected IFCs, respectively. In short, the extremely long lifetime of the ZA phonons close to Γ, combined with their nonzero group velocity [Fig. 3(a)] obtained when using raw IFCs causes the divergence of κ. We also explore the mode contribution to total thermal conductivity obtained by

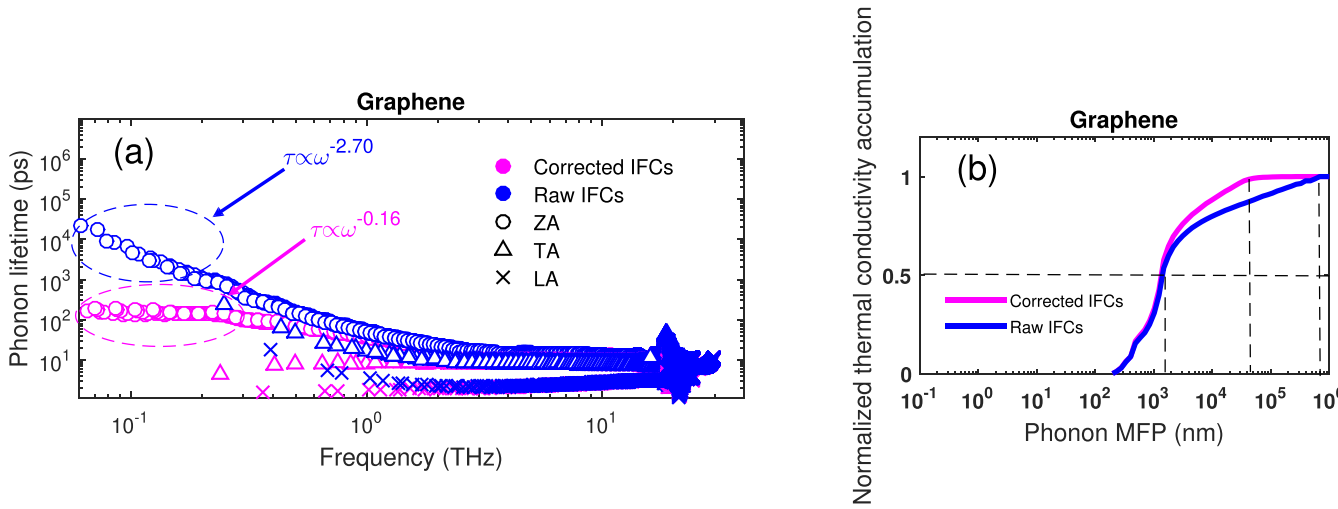

FIG. 4. (a) Lifetime of the acoustic modes in graphene from raw and corrected harmonic IFCs at 300 K. (b) Normalized thermal conductivity accumulation in graphene from corrected and raw harmonic IFCs at 300 K.

the corrected IFCs, which shows that the ZA mode is still the dominant mode in graphene with about 85% contribution. The contribution from the TA and LA modes are found to be about 12% and 3%, respectively.

Next, we consider the normalized thermal conductivity accumulation as a function of the phonon mean free path (MFP). This parameter is of particular importance for the design and tuning of the thermal conductivity of a system by changing its size. Figure 4(b) shows the normalized accumulation as a function of the phonon MFP for both corrected and raw harmonic IFCs. As a typical measure to determine what range of MFP contributes most to the κ value, the MFP responsible for 50% of the total thermal conductivity is examined, $\Lambda^{\star}$. As can be seen in Fig. 4(b), $\Lambda^{\star}$ for both corrected and raw harmonic IFCs are very similar, about 1300 nm. However, we recognize a striking difference between thermal conductivity accumulation functions of corrected and raw IFCs. Based on what the corrected IFCs predict, the thermal conductivity of graphene saturates at phonon MFP of about 42 000 nm, with practically no contribution from phonons with higher MFP. However, based on prediction of raw IFCs the saturated MFP is about 572 000 nm, one order of magnitude higher than that predicted by the corrected IFCs. We believe that such long MFP contribution is an artifact resulting from the extremely long lifetime of the ZA phonons in the long-wavelength limit together with their unphysical nonzero group velocity. This shows that correcting the harmonic IFCs can also affect the thermal conductivity accumulation function, of practical importance when designing graphene-based systems.

The uncertainty in κ prediction by the PBTE/DFT framework when using different types of XCF and PP in DFT calculations has been known as one of the drawbacks of this method. Jain and McGaughey [14] used different types of XCF-PP to calculate κ in crystalline silicon. They found that using different XCF-PP can results in about 35% discrepancy in final κ prediction. For 2D materials, the discrepancy is reported to be even worse as Ref. [11] and Ref. [12] used different XCF-PP combinations to predict κ in graphene and reported values in the range of 5442–8677 $\mathrm{W\,m^{-1}\,K^{-1}}$ [11] and 1936-4376 $\mathrm{W\,m^{-1}\,K^{-1}}$ [12]. In both studies, the relatively large discrepancy between the prediction of different XCF-PP stemmed from different phonon lifetime and the Grüneisen parameters of the ZA mode at the long-wavelength limit. Very recently, Mortazavi *el al*. [49] proposed an accelerated method based on machine-learning interatomic potentials to predict κ using the ShengBTE code. They used three different XCFs to train their data set, and found the values of 3730, 3640, and 3600 $\mathrm{W\,m^{-1}\,K^{-1}}$ for thermal conductivity of graphene, and thus concluded that unlike the prior reports [11,12], the effect of XCFs on the estimated thermal conductivity is negligible. Here, based on the results of Fig. 4(a), we suspect that the difference in lifetime observed previously by Ref. [11] and Ref. [12] at the long-wavelength limit, which in turn leads to large difference in κ when different types of XCF-PP are used, is more related to how well the ZA mode is predicted to be quadratic when $q \to 0$ in each XCF-PP, rather than the direct effect of XCF-PP used. Thus, here we compare three different XCF-PP: PBE-PAW, PBEsol-PAW, and LDA-PAW, which yield the most inconsistent results when predicting κ, according to Ref. [11]. However, in each case, after obtaining the raw IFCs from DFT, they were corrected to ensure that the ZA mode close to the Γ point is perfectly quadratic. The predicted κ values obtained this way as function of temperature between 300 K to 550 K are shown in Fig. 5. This figure also shows the κ values from raw IFCs at a dense grid of $270 \times 270 \times 1$ when the PBE-PAW combination is used in the DFT calculations. We also included two experimental results that have been usually used to evaluate the PBTE/DFT κ prediction of graphene. One of the experiments was carried out on a practically isotopically pure graphene sample (only having 0.01% C^{13}) with a size of 2.8 μm [50], the other on a larger sample of 9.7 μm [51]. Interestingly, as can be seen in Fig. 5, our findings show that the κ values predicted by different XCF-PP combinations after imposing the correction on the harmonic IFCs shows an excellent consistency with each other, and also with the experimental data. The room-temperature prediction of κ by corrected IFCs using PBE-PAW, PBEsol-PAW, and LDA-PAW combinations are 3850, 3552, and 3749 $\mathrm{W\,m^{-1}\,K^{-1}}$, respectively. These values are also in very good agreement

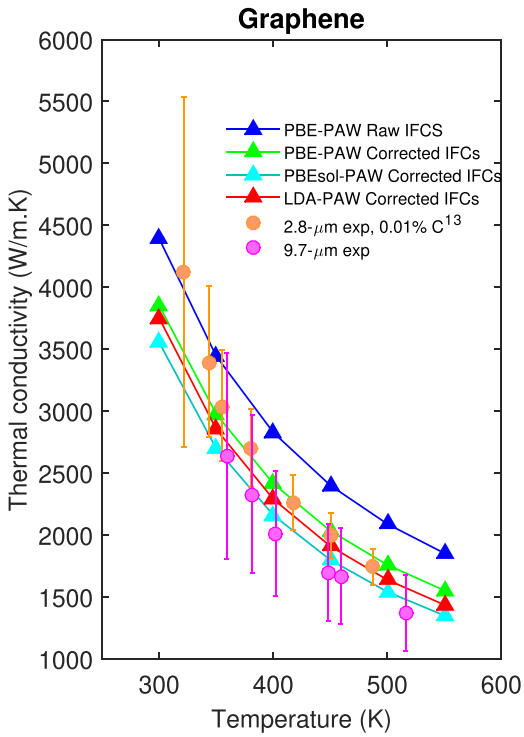

FIG. 5. Temperature dependence of the thermal conductivity in graphene from 300 K to 550 K predicted by corrected harmonic IFCs using different XC functionals. For PBE-PAW, the result from the raw harmonic IFCs at a $270 \times 270 \times 1$ **q**-point grid is also shown for comparison. The plot also shows the results from two experimental measurements on 2.8 μm [50] and 9.7 μm [51] samples.

with the method based on machine-learning interatomic potential proposed by Ref. [49]. Also, we note that considering a single XCF-PP of PBE-PAW, the predicted κ by the corrected IFCs over the temperature range studied is generally in a better agreement with experiment than that predicted by raw IFCs (Fig. 5). So, our findings suggest that postprocessing the harmonic IFCs can help to increase the accuracy in PBTE/DFT κ calculation framework, and also reduce the uncertainty when using different XCF-PP combinations. Finally, we note that the PBTE/DFT prediction of thermal conductivity presented here is based on three-phonon scattering processes. However, recent studies show that considering four-phonon scattering processes in graphene can further reduce the thermal conductivity [52], and leads to even a better agreement with experiments.

B. Silicene

Silicene, having a buckled hexagonal lattice structure, is the silicon counterpart of graphene, a member of the group-IV monolayers, which also includes germanene and stanene. Unlike graphene, which has a flat atomic structure, silicene possesses a buckled structures with a tunable electronic band gap [53]. Due to challenges in preparing freestanding silicene samples experimentally, a great deal of attention has been given to the numerical study of κ in silicene using methods such as MD [54–56] and PBTE/DFT [34,35,57,58]. However, these methods are also not exempt from inconsistency in the predicted value of κ and its convergence behavior. For example, very recently, values of 9.2 $\mathrm{W\,m^{-1}\,K^{-1}}$ [59] and 27.72 $\mathrm{W\,m^{-1}\,K^{-1}}$ [58] were predicted using the PBTE/DFT method. Here, we revisit the phonon thermal transport in silicene with a focus on the behavior of the ZA mode close to the Γ point. Figure 6(a) shows the phonon dispersion curve of silicene obtained by both corrected and raw harmonic IFCs. Similar to graphene, the acoustic modes are shown by ZA, TA, and LA. As can be seen in Fig. 6(a), the dispersion curves predicted by the corrected and raw IFCs again are almost indistinguishable, except for the ZA mode in a region very close to Γ [for example, $0 < \mathbf{q} < 0.06$, Figs. 6(b) and 6(c)]. Based on our numerical fitting, the dispersion curve obtained directly from DFT contains linear components at the long-wavelength limit as $\omega = 3.39q$, while for corrected IFCs the dependence on phonon wave vector **q** is quadratic, $\omega = 21.81q^2$. Next, we consider the phonon group velocity of the acoustic modes in silicene predicted by raw and corrected IFCs, as shown in Fig. 7(a). Similar to graphene, the most notable difference between the predicted group velocities is the nonzero group velocity of about 1.5 km/s predicted using the raw IFCs, whereas the corrected IFCs yield zero, as it should be.

Similar to graphene, the convergence of the intrinsic thermal conductivity of silicene with respect to **q**-mesh size when only three-phonon scattering processes are included has been a topic of debate. Using the iterative solution and the PBTE/DFT framework, a divergent behavior was reported by Ref. [34] and Ref. [23], while convergence has been reported by others Ref. [35,58]. Figures 7(b) and 7(c) show the variation of thermal conductivity in silicene by increasing the **q**-mesh size obtained from corrected and raw harmonic IFCs. Similar to graphene, we find that using raw IFCs, the thermal conductivity diverges even when considering a very dense **q**-mesh grid. However, κ has a well-converged behavior if corrected harmonic IFCs are used in the calculations. For comparison, we determine the room-temperature κ at a dense **q**-point grid of $200 \times 200 \times 1$, and find the the values of 22 $\mathrm{W\,m^{-1}\,K^{-1}}$ and 40 $\mathrm{W\,m^{-1}\,K^{-1}}$ by corrected and raw IFCs, respectively. We note that the value of 22 $\mathrm{W\,m^{-1}\,K^{-1}}$ agrees well with the value of about 26 $\mathrm{W\,m^{-1}\,K^{-1}}$ that is recently reported when IFCs are obtained using machine-learning interatomic potentials [49]. It is also interesting to note that, similarly to graphene, using corrected IFCs can greatly accelerate the convergence of κ. For example, a prior work used a $90 \times 90 \times 1$ **q**-grid to achieve the convergence, however, based on Fig. 7(b), we find that even a $30 \times 30 \times 1$ grid is reasonably sufficient to get a converged value. The phonon lifetime obtained by the raw and corrected IFCs in silicene is illustrated in Fig. 8(a). As opposed to graphene, it can be seen that in silicene the TA and LA modes have longer lifetime than the ZA mode, which stems from the breakdown of the mirror symmetry in silicene. Based on Fig. 8(a), using the corrected IFCs affects not only the lifetimes of the ZA mode, but also those of the TA and LA modes. For example, compared to raw IFCs, the lifetime of the long-wavelength ZA and TA modes predicted by corrected IFCs are shortened by about four and three orders of magnitude, respectively. Again, we analyze the power-law behavior for the lifetimes of the long-wavelength ZA and TA modes. Interestingly, we find that γ is about 1.0 for the ZA mode, so it cannot be

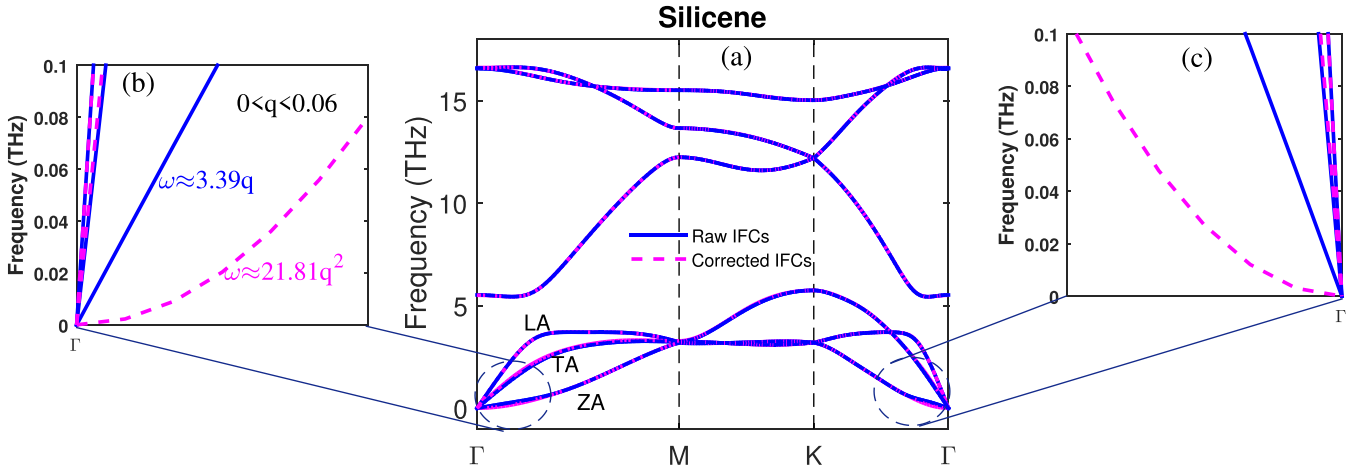

FIG. 6. (a) Phonon dispersion curve of silicene using the raw and corrected harmonic IFCs. (b) Zoomed-in dispersion close to Γ along Γ-M. (c) Zoomed-in dispersion close to Γ along Γ-K.

the reason of the κ divergence in silicene (divergence occurs for $\gamma > 2$). However, γ is found to be about 2.5 for the TA mode. Here we show that, similarly to the ZA mode [48], having $\gamma > 2$ for the TA mode in the power-law relation also results in the divergence of thermal conductivity. Let $N \times N \times 1$ be the **q**-mesh used for integration over the BZ. The smallest nonzero $|\mathbf{q}|$ associated with the choice of N is $\frac{\xi}{N}$, where ξ is a constant. Now we find the dependency of each contributing term in Eq. 1 on N for large values of N. The TA branch in the phonon dispersion curve has a linear dependence on **q** as $\mathbf{q} \to 0$. So in this limit, $\omega \propto \frac{1}{N}$. Also, due to this linear dependency, the TA group velocity at this limit should be constant and independent of N, $v \propto N^0$. Based on Eq. 1, the product $n_0(1+n_0)$, where n_0 is the equilibrium population of phonons given by $n_0 = \frac{1}{exp(\frac{\hbar\omega}{K_B T})-1}$, is another contributing factor in determining the thermal conductivity. Using the approximation $e^x \approx 1 + x$, which is valid for $x \ll 1$, it can be seen that $n_0(1+n_0) \propto N^2$. Finally, assuming the power-law relation of $\tau = \beta\omega^{-\gamma}$, we find that $\tau \propto N^{\gamma}$. substituting all these in Eq. 1 gives $\kappa \propto N^{\gamma-2}$. So, to guarantee a converging behavior for κ when $N \to \infty$, it is necessary to have $\gamma - 2 < 0$, or $\gamma < 2$. This can explain why the TA mode with a γ value of 2.5 obtained when raw IFCs are used leads to divergence of κ in silicene. However, when the corrected IFCs are used, the TA modes at the long-wavelength limit becomes almost independent of ω ($\gamma \approx 0$), and the convergence occurs as in Fig. 8(b).

We also calculate the contribution from different phonon modes in κ of silicene using corrected harmonic IFCs, and find that the ZA, TA, and LA modes contribute about 15%, 29%, and 29% to the total lattice thermal conductivity, respectively. Also, the optical modes contribute about 27%. Finally, we plot the normalized thermal conductivity accumulation function obtained by raw and corrected IFCs on a $200 \times 200 \times 1$ **q**-point grid in Fig. 8(b). It can be seen that using the corrected IFCs considerably affects the accumulation function as well. The corresponding $\Lambda^{\star}$ values (defined in Sec. III A) are determined to be about 20 nm and 75 nm for corrected and raw IFCs, respectively. Also, one can see that the corrected IFCs predict κ to saturate for MFP of about 230 nm. However, raw IFCs predicts that there are still contribution from phonons with MFP of about 89 000 nm.

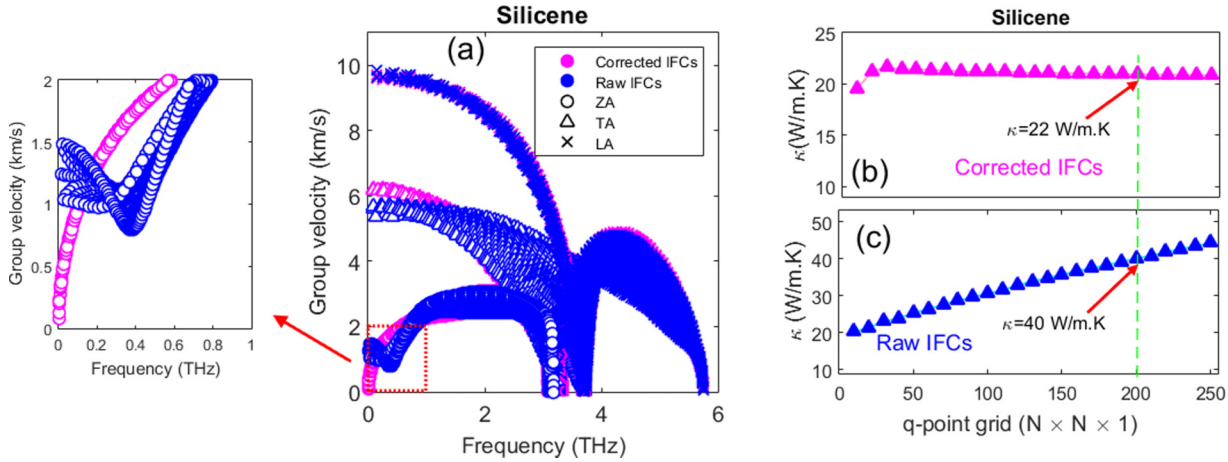

FIG. 7. (a) Group velocity of acoustic modes in silicene. [(b) and (c)] Convergence of thermal conductivity of silicene at 300 K with respect to **q**-point grid size predicted by the corrected and raw harmonic IFCs, respectively.

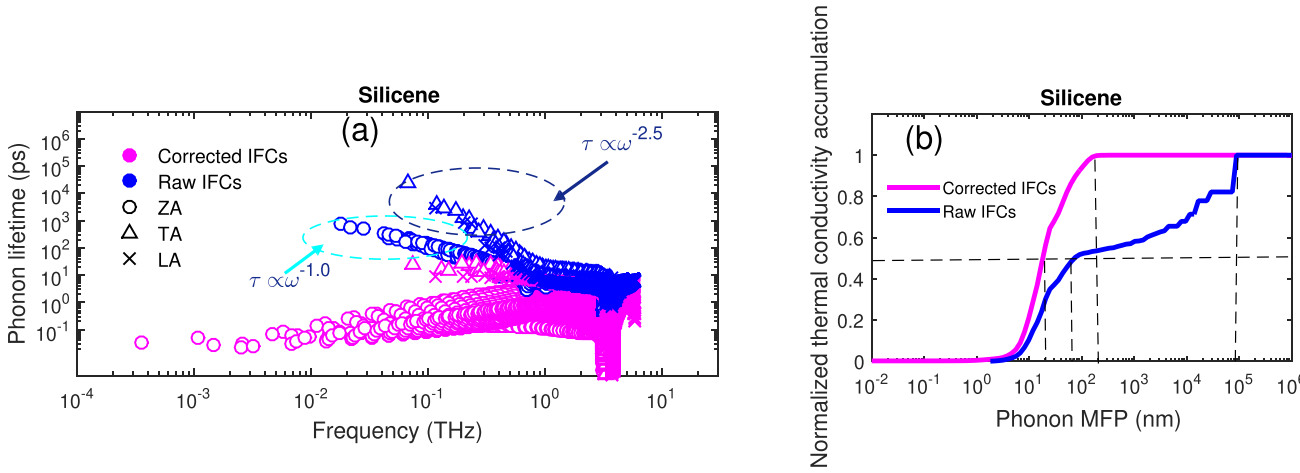

FIG. 8. (a) Lifetime of the acoustic modes in silicene from raw and corrected harmonic IFCs at 300 K. (b) Normalized thermal conductivity accumulation in silicene from corrected and raw harmonic IFCs at 300 K.

Therefore, similarly to the case of graphene, using corrected harmonic IFCs is crucial to obtaining a physically correct thermal conductivity accumulation function.

C. α-Nitrophosphorene

As an example of a 2D monolayer with a puckered structure, here we consider α-NP, which has recently attracted considerable attention due to promising properties such as improved air stability compared to black phosphorene [60,61], highly anisotropic electron mobility [61], and negative Poisson's ratio (NPR) [37]. A detailed study of the phonon thermal transport in α-NP can be found in Ref. [62]. Here, we focus on the effects that correcting the harmonic IFCs can have on predicted thermal conductivity in this monolayer. Figure 9(a) shows the dispersion curve of α-NP based on corrected and raw harmonic IFCs. As can be seen in Fig. 1(c), there are four atoms in the unit cell of α-NP, which results in three acoustic and nine optical modes in its dispersion curve. The situation in α-NP is different from graphene and silicene, as using the raw IFCs results in a U-shaped region in the dispersion curve with small, negative ZA phonon frequencies (less than 0.3 THz) along both $\Gamma - Y$ and $\Gamma - X$ directions. However, when the corrected IFCs are used the negative frequency region disappears, and the quadratic shape of the ZA mode is recovered [Figs. 9(b) and 9(c)]. Figures 10(a) and 10(b) show the calculated lattice thermal conductivity as a function of **q**-point grid size using raw and corrected harmonic IFCs and the same third-order anharmonic IFCs. Here we find that both sets of IFCs results in converged values of thermal conductivity. However, the anisotropy predicted by the corrected one is reversed compared to that predicted by the raw IFCs. Based on Fig. 10(a), the room-temperature κ value predicted by raw IFCs converges to $\kappa_{xx} = 12.2\ \mathrm{W\,m^{-1}\,K^{-1}}$ and $\kappa_{yy} = 21.2\ \mathrm{W\,m^{-1}\,K^{-1}}$, which implies $\kappa_{yy} > \kappa_{xx}$. However, based on corrected IFCs we find that $\kappa_{xx} = 36.1\ \mathrm{W\,m^{-1}\,K^{-1}}$ and $\kappa_{yy} = 18.7\ \mathrm{W\,m^{-1}\,K^{-1}}$, suggesting $\kappa_{yy} < \kappa_{xx}$. This reversed anisotropy prediction is found for the whole temperature range studied (300 K to 800 K), as illustrated in Fig. 10(c). The reversed anisotropy predicted by raw IFCs directly obtained from DFT compared to the prediction of the corrected IFCs is also reported by Ref. [21] for the case of monolayer

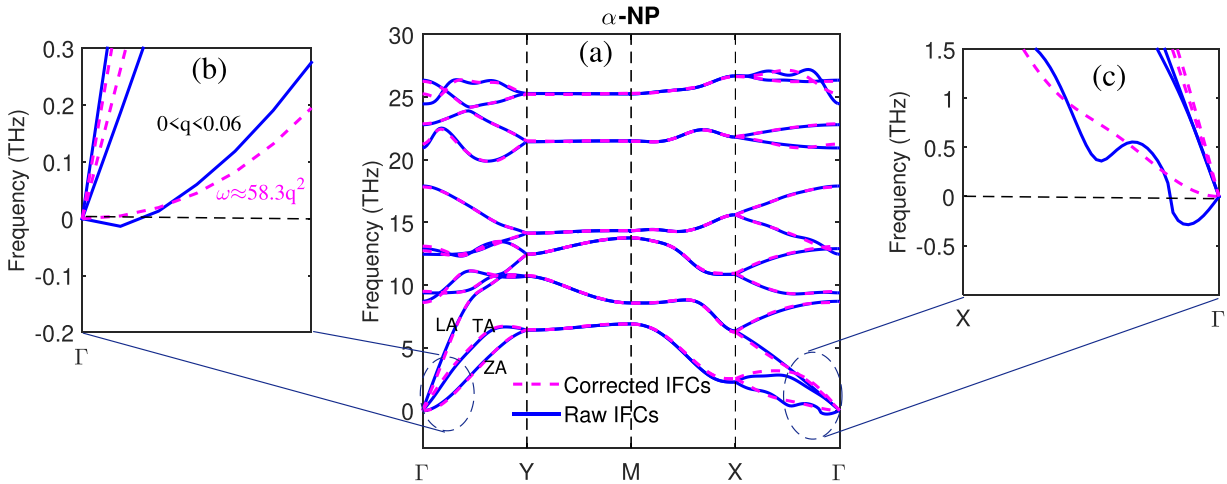

FIG. 9. (a) Phonon dispersion curve of α-NP using the raw and corrected harmonic IFCs. (b) Zoomed-in dispersion close to Γ along Γ-Y. (c) Zoomed-in dispersion close to Γ along Γ-X.

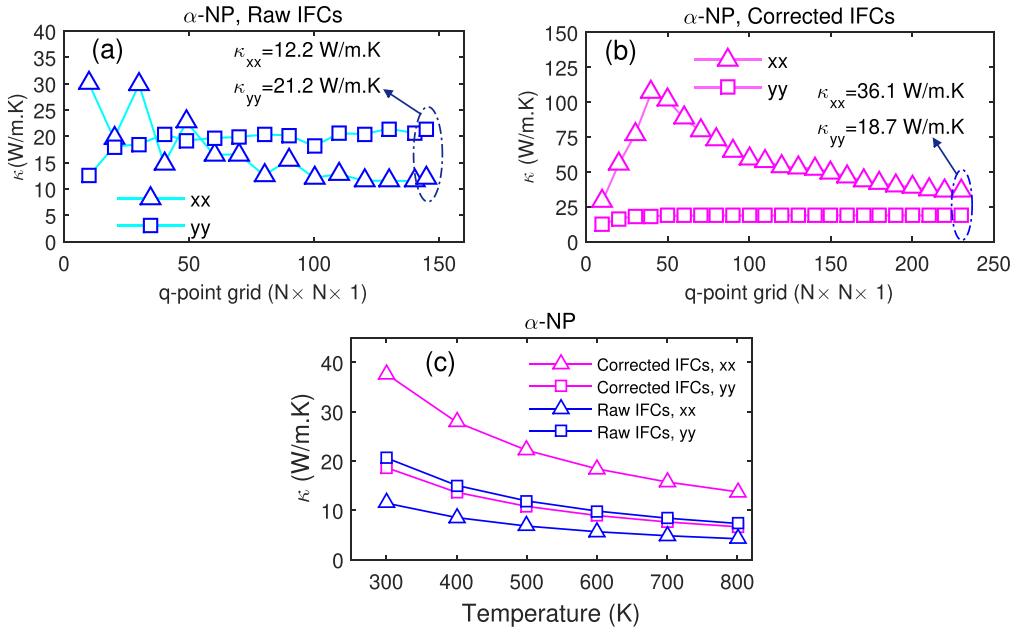

FIG. 10. [(a) and (b)] Convergence of thermal conductivity of α-NP at 300 K with respect to **q**-point grid size predicted by the corrected and raw harmonic IFCs, respectively. (c) Thermal conductivity of α-NP from 300 K to 800 K predicted by raw and corrected harmonic IFCs along the x and y directions.

borophene. Thus, using harmonic IFCs that results in negative ZA phonon frequencies (even when very small) can greatly affect the κ prediction, even to the point of reversing the anisotropy in the anisotropic systems.

IV. SUMMARY AND CONCLUSION

Solving the PBTE based on DFT is currently the most powerful theoretical tool to predict lattice thermal conductivity in a wide range of materials. To use this framework, however, obtaining an accurate phonon dispersion curve is a necessary step, which has been always challenging when considering 2D materials, particularly for the acoustic flexural ZA branch. Based on elasticity theory, the ZA branch of unstrained few-layer systems is always quadratic. However, the ZA branch calculated by commonly used DFT packages in many previous studies either has small linear components or negative frequencies. Thus, postprocessing of the raw harmonic IFCs to manually impose the rotational invariance conditions and obtain a perfectly quadratic ZA branch dispersion is necessary before any thermal conductivity calculation. Here, we systematically revisit phonon thermal transport in graphene, silicene, and α-nitrophosphorene as showcases with flat, buckled, and puckered structures to demonstrate how correcting IFCs affect κ predictions based on the PBTE/DFT method. We find that even visually small changes in the shape of the ZA branch as a result of correcting IFCs can substantially improve the PBTE/DFT results in terms of predicted κ value, convergence behavior, uncertainty in the results obtained by using different XCF-PP combinations, phonon mean free path, and predicted anisotropy. For example, in the case of silicene, we find that using the raw harmonic IFCs directly from DFT results in divergence of thermal conductivity. However, lattice thermal conductivity based on the corrected harmonic IFCs is well-converged at a $30 \times 30 \times 1$ **q**-point grid, which is much faster and computationally less expensive convergence compared to previous studies. Also, evaluated on a very dense grid of $200 \times 200 \times 1$ **q**-point, we find a 45% difference between predicted thermal conductivity of silicene by raw and corrected harmonic IFCs, with the latter in much better agreement with the prediction of recently developed approaches that incorporate machine-learning methods in DFT. Our findings can provide helpful insight for further fundamental phonon transport analysis in 2D materials.

The data that support the findings of this paper are available from the corresponding author upon reasonable request.

ACKNOWLEDGMENTS

This work was supported by the Natural Sciences and Engineering Research Council of Canada (NSERC). Computations were performed on the Niagara Supercomputer at the SciNet HPC Consortium. SciNet is funded by the Canada Foundation for Innovation under the auspices of Compute Canada; the Government of Ontario; Ontario Research Fund–Research Excellence; and the University of Toronto.

[1] P.-F. Liu, T. Bo, J. Xu, W. Yin, J. Zhang, F. Wang, O. Eriksson, and B.-T. Wang, First-principles calculations of the ultralow thermal conductivity in two-dimensional group-IV selenides, Phys. Rev. B **98**, 235426 (2018).

[2] A. A. Balandin, S. Ghosh, W. Bao, I. Calizo, D. Teweldebrhan, F. Miao, and C. N. Lau, Superior thermal conductivity of single-layer graphene, Nano Lett. **8**, 902 (2008).

[3] L. Lindsay, W. Li, J. Carrete, N. Mingo, D. A. Broido, and T. L. Reinecke, Phonon thermal transport in strained and unstrained graphene from first principles, Phys. Rev. B **89**, 155426 (2014).

[4] L. Lindsay, C. Hua, X. Ruan, and S. Lee, Survey of *ab initio* phonon thermal transport, Mater. Today Phys. **7**, 106 (2018).

[5] A. J. McGaughey, A. Jain, H.-Y. Kim, and B. Fu, Phonon properties and thermal conductivity from first principles, lattice dynamics, and the Boltzmann transport equation, J. Appl. Phys. **125**, 011101 (2019).

[6] A. Jain and A. J. McGaughey, Strongly anisotropic in-plane thermal transport in single-layer black phosphorene, Sci. Rep. **5**, 8501 (2015).

[7] A. Taheri, C. Da Silva, and C. H. Amon, Effects of biaxial tensile strain on the first-principles-driven thermal conductivity of buckled arsenene and phosphorene, Phys. Chem. Chem. Phys. **20**, 27611 (2018).

[8] A. Taheri, C. Da Silva, and C. H. Amon, Phonon thermal transport in β- NX (X = P, As, Sb) monolayers: A first-principles study of the interplay between harmonic and anharmonic phonon properties, Phys. Rev. B **99**, 235425 (2019).

[9] A. Taheri, C. Da Silva, and C. H. Amon, Highly tunable thermal conductivity of C_3N under tensile strain: A first-principles study, J. Appl. Phys. **127**, 184304 (2020).

[10] T. Ma, P. Chakraborty, X. Guo, L. Cao, and Y. Wang, First-principles modeling of thermal transport in materials: Achievements, opportunities, and challenges, Int. J. Thermophys. **41**, 9 (2020).

[11] A. Taheri, C. Da Silva, and C. H. Amon, First-principles phonon thermal transport in graphene: Effects of exchange-correlation and type of pseudopotential, J. Appl. Phys. **123**, 215105 (2018).

[12] G. Qin, Z. Qin, H. Wang, and M. Hu, On the diversity in the thermal transport properties of graphene: A first-principles-benchmark study testing different exchange-correlation functionals, Comput. Mater. Sci. **151**, 153 (2018).

[13] H. Xie, X. Gu, and H. Bao, Effect of the accuracy of interatomic force constants on the prediction of lattice thermal conductivity, Comput. Mater. Sci. **138**, 368 (2017).

[14] A. Jain and A. J. McGaughey, Effect of exchange–correlation on first-principles-driven lattice thermal conductivity predictions of crystalline silicon, Comput. Mater. Sci. **110**, 115 (2015).

[15] J. Yan, Y. Zhang, P. Kim, and A. Pinczuk, Electric Field Effect Tuning of Electron-Phonon Coupling in Graphene, Phys. Rev. Lett. **98**, 166802 (2007).

[16] R. Duggal and M. Pasquali, Dynamics of Individual Single-Walled Carbon Nanotubes in Water by Real-Time Visualization, Phys. Rev. Lett. **96**, 246104 (2006).

[17] Y. Wei, B. Wang, J. Wu, R. Yang, and M. L. Dunn, Bending rigidity and gaussian bending stiffness of single-layered graphene, Nano Lett. **13**, 26 (2013).

[18] L. Landau and E. Lifshitz, *Theory of Elasticity* (Pergamon, Oxford, 1995).

[19] M. Mohr, J. Maultzsch, E. Dobardžić, S. Reich, I. Milošević, M. Damnjanović, A. Bosak, M. Krisch, and C. Thomsen, Phonon dispersion of graphite by inelastic x-ray scattering, Phys. Rev. B **76**, 035439 (2007).

[20] Y. Kuang, L. Lindsay, Q. Wang, and L. He, Lattice chain theories for dynamics of acoustic flexural phonons in nonpolar nanomaterials, Phys. Rev. B **102**, 144301 (2020).

[21] J. Carrete, W. Li, L. Lindsay, D. A. Broido, L. J. Gallego, and N. Mingo, Physically founded phonon dispersions of few-layer materials and the case of borophene, Mater. Res. Lett. **4**, 204 (2016).

[22] A. Manjanath, V. Kumar, and A. K. Singh, Mechanical and electronic properties of pristine and Ni-doped Si, Ge, and Sn sheets, Phys. Chem. Chem. Phys. **16**, 1667 (2014).

[23] X. Gu and R. Yang, First-principles prediction of phononic thermal conductivity of silicene: A comparison with graphene, J. Appl. Phys. **117**, 025102 (2015).

[24] X. Fan, W. Zheng, J.-L. Kuo, and D. J. Singh, Structural stability of single-layer MoS_2 under large strain, J. Phys.: Condens. Matter **27**, 105401 (2015).

[25] A. Berkdemir, H. R. Gutiérrez, A. R. Botello-Méndez, N. Perea-López, A. L. Elías, C.-I. Chia, B. Wang, V. H. Crespi, F. López-Urías, J.-C. Charlier *et al.*, Identification of individual and few layers of WS_2 using Raman spectroscopy, Sci. Rep. **3**, 1755 (2013).

[26] U. Choudhry, S. Yue, and B. Liao, Origins of significant reduction of lattice thermal conductivity in graphene allotropes, Phys. Rev. B **100**, 165401 (2019).

[27] W.-X. Zhou and K.-Q. Chen, First-principles determination of ultralow thermal conductivity of monolayer WSe_2, Sci. Rep. **5**, 15070 (2015).

[28] X. Zhang, H. Xie, M. Hu, H. Bao, S. Yue, G. Qin, and G. Su, Thermal conductivity of silicene calculated using an optimized stillinger-weber potential, Phys. Rev. B **89**, 054310 (2014).

[29] L. Zhu, G. Zhang, and B. Li, Coexistence of size-dependent and size-independent thermal conductivities in phosphorene, Phys. Rev. B **90**, 214302 (2014).

[30] A. Molina-Sanchez and L. Wirtz, Phonons in single-layer and few-layer Mo_2 and WS_2, Phys. Rev. B **84**, 155413 (2011).

[31] M. Born and K. Huang, *Dynamical Theory of Crystal Lattices* (Clarendon Press, Oxford, 1954).

[32] D. C. Gazis and R. F. Wallis, Conditions for rotational invariance of a harmonic lattice, Phys. Rev. **151**, 578 (1966).

[33] S.-F. Wang, H.-L. Zhang, and X.-Z. Wu, A new rotation sum rule for the atomic force constants, J. Phys.: Condens. Matter **19**, 386233 (2007).

[34] H. Xie, T. Ouyang, É. Germaneau, G. Qin, M. Hu, and H. Bao, Large tunability of lattice thermal conductivity of monolayer silicene via mechanical strain, Phys. Rev. B **93**, 075404 (2016).

[35] Y. Kuang, L. Lindsay, S.-Q. Shi, and G. Zheng, Tensile strains give rise to strong size effects for thermal conductivities of silicene, germanene and stanene, Nanoscale **8**, 3760 (2016).

[36] See Supplemental Material at http://link.aps.org/supplemental/10.1103/PhysRevB.103.235426 for a discussion on the effects of harmonic IFCs correction on phonon dispersion and the thermal conductivity of black phosphorene.

[37] W.-Z. Xiao, G. Xiao, Q.-Y. Rong, and L.-L. Wang, Theoretical discovery of novel two-dimensional V^A-N binary compounds with auxiticity, Phys. Chem. Chem. Phys. **20**, 22027 (2018).

[38] F. Ersan, E. Aktürk, and S. Ciraci, Stable single-layer structure of group-v elements, Phys. Rev. B **94**, 245417 (2016).

[39] B. Peng, D. Zhang, H. Zhang, H. Shao, G. Ni, Y. Zhu, and H. Zhu, The conflicting role of buckled structure in phonon transport of 2D group-IV and group-V materials, Nanoscale **9**, 7397 (2017).

[40] A. Togo, F. Oba, and I. Tanaka, First-principles calculations of the ferroelastic transition between rutile-type and $CaCl_2$-type SiO_2 at high pressures, Phys. Rev. B **78**, 134106 (2008).

[41] F. Eriksson, E. Fransson, and P. Erhart, The Hiphive package for the extraction of high-order force constants by machine learning, Adv. Theory Simul. **2**, 1800184 (2019).

[42] W. Li, J. Carrete, N. A. Katcho, and N. Mingo, Shengbte: A solver of the Boltzmann transport equation for phonons, Comput. Phys. Commun. **185**, 1747 (2014).

[43] P. Hess, Thickness of elemental and binary single atomic monolayers, Nanoscale Horiz. **5**, 385 (2020).

[44] S. Ma, C. He, L. Sun, H. Lin, Y. Li, and K. Zhang, Stability of two-dimensional PN monolayer sheets and their electronic properties, Phys. Chem. Chem. Phys. **17**, 32009 (2015).

[45] X. Xu, L. F. Pereira, Y. Wang, J. Wu, K. Zhang, X. Zhao, S. Bae, C. T. Bui, R. Xie, J. T. Thong *et al.*, Length-dependent thermal conductivity in suspended single-layer graphene, Nat. Commun. **5**, 3689 (2014).

[46] W.-R. Zhong, M.-P. Zhang, B.-Q. Ai, and D.-Q. Zheng, Chirality and thickness-dependent thermal conductivity of few-layer graphene: A molecular dynamics study, Appl. Phys. Lett. **98**, 113107 (2011).

[47] Luiz Felipe C. Pereira and D. Donadio, Divergence of the thermal conductivity in uniaxially strained graphene, Phys. Rev. B **87**, 125424 (2013).

[48] Y. Kuang, L. Lindsay, S. Shi, X. Wang, and B. Huang, Thermal conductivity of graphene mediated by strain and size, Int. J. Heat Mass Transf. **101**, 772 (2016).

[49] B. Mortazavi, E. V. Podryabinkin, I. S. Novikov, T. Rabczuk, X. Zhuang, and A. V. Shapeev, Accelerating first-principles estimation of thermal conductivity by machine-learning interatomic potentials: A MTP/ShengBTE solution, Comput. Phys. Commun. **258**, 107583 (2021).

[50] S. Chen, Q. Wu, C. Mishra, J. Kang, H. Zhang, K. Cho, W. Cai, A. A. Balandin, and R. S. Ruoff, Thermal conductivity of isotopically modified graphene, Nat. Mater. **11**, 203 (2012).

[51] S. Chen, A. L. Moore, W. Cai, J. W. Suk, J. An, C. Mishra, C. Amos, C. W. Magnuson, J. Kang, L. Shi *et al.*, Raman measurements of thermal transport in suspended monolayer graphene of variable sizes in vacuum and gaseous environments, ACS nano **5**, 321 (2011).

[52] T. Feng and X. Ruan, Four-phonon scattering reduces intrinsic thermal conductivity of graphene and the contributions from flexural phonons, Phys. Rev. B **97**, 045202 (2018).

[53] T. P. Kaloni, Y. Cheng, and U. Schwingenschlögl, Hole doped dirac states in silicene by biaxial tensile strain, J. Appl. Phys. **113**, 104305 (2013).

[54] Q.-X. Pei, Y.-W. Zhang, Z.-D. Sha, and V. B. Shenoy, Tuning the thermal conductivity of silicene with tensile strain and isotopic doping: A molecular dynamics study, J. Appl. Phys. **114**, 033526 (2013).

[55] H.-p. Li and R.-q. Zhang, Vacancy-defect–induced diminution of thermal conductivity in silicene, Europhys. Lett. **99**, 36001 (2012).

[56] T. Y. Ng, J. Yeo, and Z. Liu, Molecular dynamics simulation of the thermal conductivity of shorts strips of graphene and silicene: A comparative study, Int. J. Mech. Mater. Des. **9**, 105 (2013).

[57] H. Xie, M. Hu, and H. Bao, Thermal conductivity of silicene from first-principles, Appl. Phys. Lett. **104**, 131906 (2014).

[58] B. Peng, H. Zhang, H. Shao, Y. Xu, R. Zhang, H. Lu, D. W. Zhang, and H. Zhu, First-principles prediction of ultralow lattice thermal conductivity of dumbbell silicene: A comparison with low-buckled silicene, ACS Appl. Mater. Interfaces **8**, 20977 (2016).

[59] N. Gupta and R. Verma, First-principles study of thermoelectric transport properties in low-buckled monolayer silicene, Physica B: Condens. Matter **606**, 412715 (2021).

[60] L. Zhao, W. Yi, J. Botana, F. Gu, and M. Miao, Nitrophosphorene: A 2D semiconductor with both large direct gap and superior mobility, J. Phys. Chem. C **121**, 28520 (2017).

[61] Y. Chen, Z. Lao, B. Sun, X. Feng, S. A. Redfern, H. Liu, J. Lv, H. Wang, and Z. Chen, Identifying the ground-state NP sheet through a global structure search in two-dimensional space and its promising high-efficiency photovoltaic properties, ACS Mater. Lett. **1**, 375 (2019).

[62] A. Taheri and C. V. Singh, Anisotropic phonon thermal transport in nitrophosphorene monolayer, Phys. Rev. Mater. **5**, 034009 (2021).